Multiple sulfur isotopes in methane seep carbonates track unsteady sulfur cycling during anaerobic methane oxidation

Antoine Crémière[1,2,3*], André Pellerin[4], Boswell Wing[5], Aivo Lepland[1,2]

[1] Geological Survey of Norway, 7491 Trondheim, Norway

[2] Centre for Arctic Gas Hydrate, Environment and Climate, University of Tromsø, 9037 Tromsø, Norway

[3] Division of Geological and Planetary Sciences, California Institute of Technology, Pasadena, California, USA

[4] Center for Geomicrobiology, Department of Biological Sciences, Aarhus University, Ny Munkegade 114, 8000 Aarhus C, Denmark

[5] Geological Sciences, University of Colorado Boulder UCB 399, Boulder, CO 80309-0399, USA

*corresponding author: cremiere@caltech.edu

Abstract

The anaerobic oxidation of methane coupled with sulfate reduction (AOM-SR) is a major microbially-mediated methane consuming process in marine sediments including methane seeps. The AOM-SR can lead to the formation of methane-derived authigenic carbonates which entrap sulfide minerals (pyrite) and carbonate-associated sulfate (CAS). We studied the sulfur isotope compositions of the pyrite and CAS in seafloor methane-derived authigenic carbonate crust samples from the North Sea and Barents Sea which reflect the time-integrated metabolic activity of the AOM-SR community as well as the physical conditions under which those carbonates are formed. In these samples, pyrite exhibits $\delta^{34}S$ values ranging from -23.4 ‰ to 14.8 ‰ and $\Delta^{33}S$ values between -0.06 ‰ and 0.16 ‰, whereas CAS is characterized by $\delta^{34}S$ values ranging from 26.2 ‰ to 61.6 ‰ and $\Delta^{33}S$ mostly between -0.05 ‰ and 0.07 ‰. Such CAS sulfur isotope compositions are distinctly lower in $\delta^{34}S$-$\Delta^{33}S$ space from published porewater sulfate values from environments where the reduction of sulfate is mostly coupled to sedimentary organic matter oxidation. Mass-balance modeling suggests that (1) AOM-SR appears to cause rapid carbonate precipitation under high methane flux near or at the sediment-water interface and (2) that the precipitation of pyrite and carbonates are not necessarily synchronous. The sulfur isotopic composition of pyrite is interpreted to reflect more variable precipitating conditions of evolving sulfide with porewater connectivity, fluctuating methane fluxes and oxidative sulfur cycle. Taken together, the multiple isotopic compositions of pyrite and sulfate in methane-derived authigenic carbonates indicate protracted precipitation under conditions of non-steady state methane seepage activity.

Keywords: anaerobic oxidation of methane, microbial sulfate reduction, multiple sulfur isotopes, methane-derived authigenic carbonates, pyrite and carbonate-associated sulfate.

1. Introduction

Marine sediments are the world's largest reservoir of methane, a potent greenhouse gas, where it occurs as dissolved, free gas and solid gas hydrate (Ruppel and Kessler, 2017). This methane is generated from organic matter either by methanogenic archaea in anaerobic sediments or by thermocatalytic cracking at depth (Claypool and Kvenvolden, 1983). On a global scale, it is estimated that more than 80 % of the methane migrating upward through the sedimentary column is consumed at the sulfate-methane transition (SMT, Fig. 1a) through the anaerobic oxidation of methane coupled to reduction of sulfate (AOM-SR) (Boetius et al., 2000; Egger et al., 2018). AOM-SR is thus a major biogeochemical sink of global importance in the methane cycle which follows the reaction:

$$CH_4 + SO_4^{2-} \rightarrow HCO_3^- + HS^- + H_2O$$

AOM-SR is microbially mediated by consortia of syntrophic anaerobic methanotrophic archaea (ANME) and sulfate-reducing deltaproteobacteria (Boetius et al., 2000; Knittel et al., 2018). However, the exact mechanism of electron balance between ANME and SRB partners has been a long-standing debate (Knittel et al., 2018; McGlynn et al., 2015; Wegener et al., 2015). To date, the leading model of metabolic interactions (Fig. 1b) relies on direct interspecies electron transfer between ANME and SRB through outer membrane multi-heme cytochromes (McGlynn et al., 2015) or conductive pili (Wegener et al., 2015). Despite these outstanding efforts expended into developing a mechanistic understanding of AOM-SR, the nature of the process in sedimentary environments remains poorly constrained (Knittel et al., 2018).

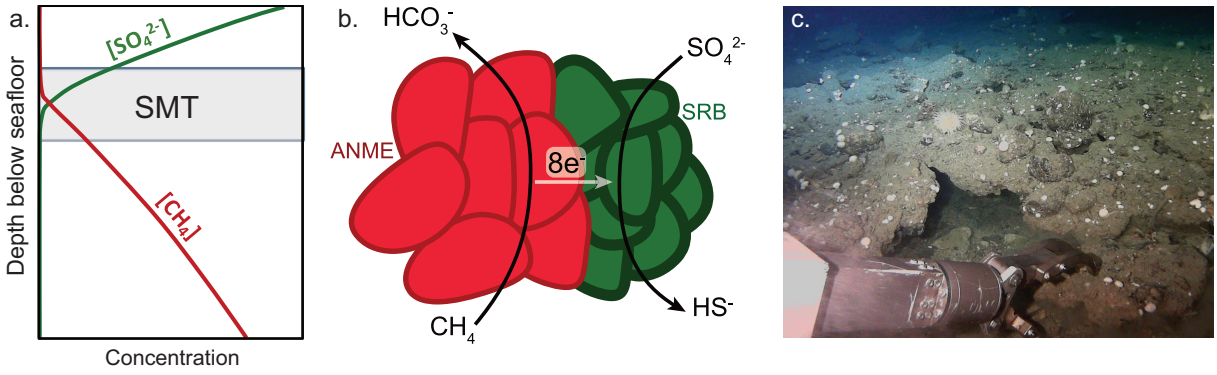

Figure 1: a. Schematic porewater profile of the sulfate-methane transition (SMT), the locus of AOM-SR. Note that depth and concentrations are not to scale. b. Most accepted syntrophic model for anaerobic oxidation of methane coupled to sulfate reduction (after McGlynn et al., 2015, Wegener et al., 2015) where electrons are directly transferred between anaerobic methanotrophic archaea (ANME) and sulfate-reducing deltaproteobacteria (SRB). c. Photo showing sampling of massive carbonate crusts covering the seafloor at the methane seep in the Barents Sea.

The isotopic composition of the most abundant stable sulfur isotopes ($^{34}S/^{32}S$) has been extensively employed to investigate sulfur cycling in modern and ancient marine environments (Jørgensen et al., 2019) including methane seeps (e.g. Aharon and Fu, 2000; Borowski et al., 2013; Gong et al., 2018; Lin et al., 2017). The magnitude of the $^{34}S/^{32}S$ isotope fractionation ($\alpha_{SR} = \frac{{}^{34}S/{}^{32}S}{{}^{34}SO_4^{2-}/{}^{32}SO_4^{2-}}$) can be as high as 0.93 (Sim et al., 2011) and likely reflect the balance between forward and backward intracellular metabolite fluxes since it is inversely proportional to cell-specific sulfate reduction rates (Brunner et al., 2012; Wing and Halevy, 2014). In contrast to sulfate reduction, the pathways for sulfide oxidation and sulfur disproportionation are less well-constrained. Distinguishing sulfide oxidation from coexisting sulfate reduction is challenging because sulfide oxidation is assumed to generate small $^{34}S/^{32}S$ fractionations (Farquhar et al., 2003; Johnston et al., 2005a; Pellerin et al., 2015). In some environments, sulfide oxidation may generate large fractionations which adds to the difficulty of separating sulfate reduction and sulfide oxidation (Pellerin et al., 2019). On the other hand, microbial culture experiments of sulfate-reducing and sulfur-disproportionating microorganisms have revealed distinct paired $^{34}S/^{32}S$ and $^{33}S/^{32}S$ isotopic fractionations

(Farquhar et al., 2003; Johnston et al., 2005a), enabling the use of multiple sulfur isotopes as additional constraints on the nature of sulfur cycling (e.g. Johnston et al., 2005b; Pellerin et al., 2015). While continuous high-pressure sediment incubation reveal that $^{34}S/^{32}S$ fractionations produced during AOM-SR is dependent on methane concentration (Deusner et al., 2014) and covers most of the range measured in laboratory and natural environments (Sim et al., 2011), experimental constrains on multiple sulfur isotope (^{33}S and ^{36}S) fractionations during AOM-SR are, to date, lacking.

Authigenic barites forming at methane seep, which have the potential to capture porewater sulfate at the SMT, show a negative $\Delta^{33}S$-$\delta^{34}S$ correlation that is distinct from porewater sulfate in environments dominated by organoclastic sulfate reduction (OSR) (Gong et al., 2018). Mass-balance calculations on sedimentary pyrite also imply that AOM-SR at depth yields sulfide with high $\delta^{34}S$ and $\Delta^{33}S$ values, different from pyrite in the overlying sediments produced by a combination of OSR and sulfur disproportionation (Lin et al., 2017). While authigenic barite can be assumed to be a robust proxy of porewater sulfate at the SMT, its voluminous precipitation at methane seeps is not commonly observed since it necessitates enhanced remobilization of barite from organic-rich sediments (Greinert et al., 2002). Porewater sulfate and its $\delta^{34}S$ and $\delta^{18}O$ signatures during AOM-SR can also be reconstructed by using carbonate-associated sulfate (CAS) trapped in methane-derived authigenic carbonates (MDACs) that precipitate ubiquitously as byproducts of AOM-SR at methane seeps (Feng et al., 2016). Moreover, MDACs offer also the possibility to study the sulfide produced by AOM-SR as it can get trapped as authigenic pyrite within the MDACs (Peckmann et al., 2001). In this study, the multiple sulfur isotopes of CAS and pyrite in methane seeps MDACs from the North Sea and Barents Sea are investigated as metabolic proxies of AOM-SR as well as to constrain the geochemical environments of MDAC formation.

2. Geological settings

The North Sea and Barents Sea have a complex geological history in which Caledonian orogenesis and Late Palaeozoic to Mesozoic basin rifts have played a major role in their genesis (Faleide et al., 1993). Both these epicontinental seas present well-developed fault systems and are recognized as petroleum provinces with several source rocks, the late Jurassic to early Cretaceous organic-rich shales being some of the most widely distributed (Doré, 1995). Over the Quaternary, these areas have experienced glaciations with several episodes of Scandinavian ice-sheet advance and retreat with subsequent surface sediments reworking and erosion leaving topographic features like plough marks, paleo ice streams or melt water channels (Winsborrow et al., 2010). Fluid flow features such as pipes, chimneys and gas accumulation as well as seafloor pockmarks (Hovland et al., 1984; Rise et al., 2014) and water column gas flares have been observed in both North Sea and Barents Sea (Crémière et al., 2016b, 2016a).

3. Material and methods

3.1. Studied samples

We studied a total of 28 individual MDAC crust samples, collected at the seafloor by remotely operated vehicle (ROV) during two research cruises dedicated to the study of hydrocarbon seepage along the Norwegian continental margin (Fig. 1c). The North Sea MDACs were sampled along a subglacial melt water channel (Alvheim channel) in which two active pockmarks with water column gas flares were observed (Crémière et al., 2016b) whereas in the south-western Barents Sea (area called Loppa High), MDACs were collected in 4 different areas where gas flares in the water column were also observed (Crémière et al., 2016a). The total carbonate content mostly ranges from 38 to 84 w.t. % with aragonite, being

typically more abundant authigenic phase than Mg-calcite. Minor amounts (<2 w.t. %) of bioclasts are also present (Crémière et al., 2016b, 2016a). Microcrystalline aragonite and Mg-calcite occur as cements filling the pore space of the seafloor sandy or muddy sediment. Aragonite is also found as detritus-free layered cement filling mm- to cm-scale cavities. The microcrystalline cement constitutes the volumetrically dominant (> ~ 90%) fraction in samples from the North Sea while samples from the Barents Sea typically contain a higher proportion (up to ~60 %) of aragonitic void-filling cement (Fig. S1). Petrographic observations show that disseminated framboidal pyrite is mostly associated with microcrystalline cements, particularly with Mg-calcite, and void-filling aragonite cement is typically devoid of pyrite (Fig. S2). The REE characteristics of the void-filling cement indicate precipitation under seawater dominated conditions whereas microcrystalline cement formed under diagenetic conditions where the fluid inventory was affected by iron reduction (Crémière et al., 2016b). The dominance of aragonite has been interpreted as an indication of precipitation under high methane fluxes supporting high metabolic AOM-SR rates close to or at the sediment-water interface.

3.2. Multiple sulfur isotopes

MDAC samples selected for the study were first cleaned from uncemented sediments and biological remains and then powdered. Splits from the same homogenized powder, typically ranging from ~20 to 100 g, were made for the extraction of pyrite and CAS. Due to relatively large sample sizes required for CAS extraction different carbonate cement types are integrated into the bulk sample. The pyrite was extracted with the chromium-reducible sulfur (CRS) method using ~2 g of powder. Acid-volatile sulfide (AVS), which was not collected, was released by an initial HCl treatment for 3 h under N_2 gas stream, then, the powder was boiled with 1M Cr-reducing solution for 5 h in order to liberate sulfur from pyrite as H_2S gas. The

158 H_2S gas was carried through a N_2 gas stream and was bubbled through a Zn-acetate solution
159 where it was quantitatively converted to ZnS.
160 For the CAS extraction, 6 to 53 g of powder was first rinsed with a large excess of 10 %
161 NaCl solution for 24 hours and then washed two times with Milli-Q water in order to remove
162 water soluble sulfate. Elemental sulfur was eliminated by rinsing the powder with acetone for
163 24 hours and a subsequent rinse with Milli-Q water. Organic matter and pyrite were oxidized
164 using 30 % H_2O_2 for 48 hours followed by multiple rinses with Milli-Q water. Finally, CAS
165 was separated by dissolving the residue in 6N HCl over 2 hours followed by filtration and
166 addition of a saturated $BaCl_2$ solution to precipitate CAS as barite in the filtrate. Dried $BaSO_4$
167 precipitate was weighed to estimate CAS concentration and then reacted with Thode reagent
168 under constant N_2 flux to release H_2S that was trapped as ZnS in a Zn-acetate trap.
169 The ZnS precipitate, derived either from CAS or CRS extractions, was filtered and
170 converted into a silver sulfide precipitate by adding 0.2 M $AgNO_3$ dropwise on the filter and
171 rinsed with 5 % NH_4OH solution followed by Milli-Q water and placed in a drying oven at
172 80°C overnight. Approximately 1 to 6 mg of Ag_2S samples were reacted with $F_{2(g)}$ in nickel
173 bombs at 250 °C, to generate $SF_{6(g)}$. The $SF_{6(g)}$ was purified via gas chromatography and its
174 isotopic composition analyzed on a Thermo MAT-253 in dual inlet mode in the Stable Isotope
175 Laboratory at McGill University. Results were normalized to repeated measurements of
176 international reference material IAEA-S-1, with a defined $\delta^{34}S$ value of -0.3 ‰ Vienna
177 Canyon Diablo Troilite (VCDT) whereas $\delta^{33}S$ value of IAEA-S-1 was taken to be -0.061 ‰
178 VCDT. Total procedural uncertainty is estimated to be lower than 0.1 ‰ for $\delta^{34}S$ and 0.01 ‰
179 for $\Delta^{33}S$, except for small samples (<1 μmol S) when the microvolume was used (uncertainty
180 for $\delta^{34}S \sim 0.5$ ‰ and $\Delta^{33}S \sim 0.05$ ‰). A summary of those analyses can be found in
181 supplements.
182 Sulfur isotope ratios are reported in delta notation:

183 $$\delta^{3i}S = \left(\frac{^{3i}R_{sample} - {}^{3i}R_{VCDT}}{^{3i}R_{VCDT}}\right) \times 1000\ (‰)$$

184 where ^{3i}R is $^{3i}S/^{32}S$ with $3i$ = 34 or 33 and VCDT refers to the international reference Vienna
185 Cañon Diablo Troilite. The capital delta notation is a measure of the deviation between the
186 $^{33}S/^{32}S$ and $^{34}S/^{32}S$ isotope ratios from the reference relationship of 0.515:

187 $$\Delta^{33}S = \delta^{33}S - 1000 \times \left(\left(1 + \frac{\delta^{34}S}{1000}\right)^{0.515} - 1\right) \times 1000\ (‰)$$

188 The sulfur isotope fractionation factor $^{3i}\alpha$ is expressed as follow:

189 $$^{3i}\alpha = \frac{^{3i}R_{H_2S/pyrite}}{^{3i}R_{SO_4^{2-}/CAS}}$$

190 with $3i$ = 34 or 33. The fractionation factors between sulfur isotopologues are related by $^{33}\lambda$:

191 $$^{33}\lambda = \frac{\ln^{33}\alpha}{\ln^{34}\alpha}$$

192 # 4. Results and Discussion

193 4.1. The nature of sulfur cycling during the formation of MDAC crusts

194 Sulfate consumption in marine sediments is typically driven by the flux of organic
195 material to the seafloor that controls the OSR (Bowles et al., 2014). However, in areas of
196 active methane seepage (with the potential exception of oil and wet gas seeps) where upward
197 migration of methane-rich fluids drives fast metabolic rates of AOM, SR can be mostly
198 coupled to AOM (Wallmann et al., 2006). In contrast to the high AOM-SR rates observed in
199 active methane seepage areas (Knittel et al., 2018; Sauer et al., 2016), background rates of
200 OSR in non-seep areas in the North Sea and Barents Sea are low (Mazzini et al., 2016; Nickel
201 et al., 2012), most likely due to the organic-poor nature of sediments. High AOM-SR rates at
202 studied seepage areas are also indicated by ubiquitous aragonite dominated MDAC crusts
203 precipitating near to or at the sediment-water interface (Luff et al., 2004) as well as by their

^{13}C-depleted carbon isotope composition with $\delta^{13}C$ values ranging from -58 to -22 ‰ VPDB (Fig. 2a)(Crémière et al., 2016b, 2016a)[30,31].

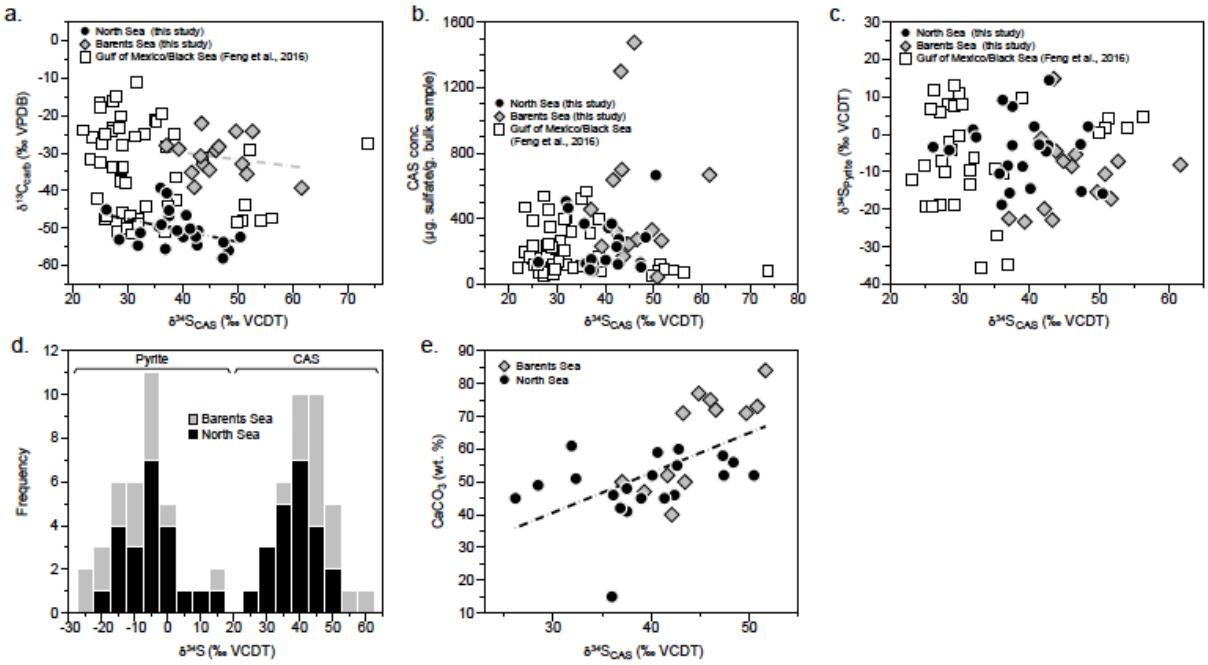

Figure 2: Geochemical results from methane-derived authigenic carbonates from the Norwegian margin compared to data from Feng et al. (2016). (a) $\delta^{13}C_{carbonate}$ against $\delta^{34}S_{CAS}$. Note that the difference in $\delta^{13}C$ values of carbonates between the Barents Sea and North Sea reflects the influence of thermogenic and microbial methane, respectively (Crémière 2016a, 2016b). (b) CAS concentration (µg. sulfate/g. bulk sample) against $\delta^{34}S_{CAS}$. (c) $\delta^{34}S_{pyrite}$ against $\delta^{34}S_{CAS}$. (d) Histogram of $\delta^{34}S$ values for pyrite and for CAS (5 ‰ bins). (e) Carbonate content against $\delta^{34}S_{CAS}$.

While the sulfur isotopic composition of dissolved sulfide is conventionally assumed to be preserved in pyrite (Wilkin and Barnes, 1996), sulfate interpretation from CAS in MDACs needs to be evaluated carefully due to possible contribution to extracted sulfate from oxidation of co-occurring sulfides prior and during sample preparation (Marenco et al., 2008). Several lines of evidence suggest that the CAS dataset is primarily derived from structurally substituted sulfate in MDACs. In our dataset, all $\delta^{34}S$ values of CAS are higher than seawater $\delta^{34}S$ (21.2 ‰; Tostevin et al., 2014) and the CAS concentrations and $\delta^{34}S$ values are comparable to recently published CAS data from MDACs screened for low pyrite content (Feng et al., 2016; Fig. 2b). In addition, there is no consistent relationship between $\delta^{34}S$ values of CAS and its concentration (Fig. 2b) or the $\delta^{34}S$ values of associated pyrite (Fig. 2c),

223 as might be expected for a substantial contribution from oxidized sulfide. Although minor
224 sulfate derived from oxidized sulfide cannot be excluded, we propose that the CAS data
225 essentially reflect the sulfur isotope composition of porewater sulfate at the time of carbonate
226 precipitation.

227 The $\delta^{34}S$ of pyrite and CAS show a bimodal distribution around seawater (Fig. 2d)
228 with values ranging from -23.4 to 14.8 ‰ (mean = -6.9 ± 9.7 ‰) and from 26.2 to 61.6 ‰
229 (mean = 42.0 ± 7.1 ‰), respectively. These results are consistent with evolving pore water at
230 methane seeps where sulfide is depleted in ^{34}S relative to seawater but where the consumption
231 of sulfate by AOM-SR exceeds its replenishment and leads to an increase in the $\delta^{34}S$ values of
232 the residual sulfate. Isotope mass balance results in the $\delta^{34}S$ of sulfide, and thus pyrite,
233 tending towards the original isotopic composition of the seawater sulfate (Aharon and Fu,
234 2000; Deusner et al., 2014; Jørgensen et al., 2004). The intensity of methane flux delivered to
235 subsurface sediments is thought to exert a major control on rates of AOM-SR (Aharon and
236 Fu, 2000; Deusner et al., 2014). Thus, under high methane efflux associated with MDAC
237 precipitation, rapid SR turnovers are thought to induce relatively small $^{34}\alpha_{AOM\text{-}SR}$ on the order
238 of 0.99 to 0.97 (Aharon and Fu, 2000; Deusner et al., 2014). While pyrite enriched in ^{34}S
239 records the locus of SMT at depth (Borowski et al., 2013; Jørgensen et al., 2004; Lin et al.,
240 2016), the formation of aragonite dominated microcrystalline cement close to the sediment-
241 water interface might limit the impact of distillation effects on sulfur isotope compositions.
242 Conversely, the decrease in permeability during MDAC cementation might lead to partial
243 isolation from bottom water, with a corresponding enrichment in ^{34}S in the residual sulfate
244 pool. This process might be reflected by weak tendency of $\delta^{34}S$ values in CAS to increase
245 with decreasing $\delta^{13}C$ values or with increasing carbonate content (Fig. 2a & f).

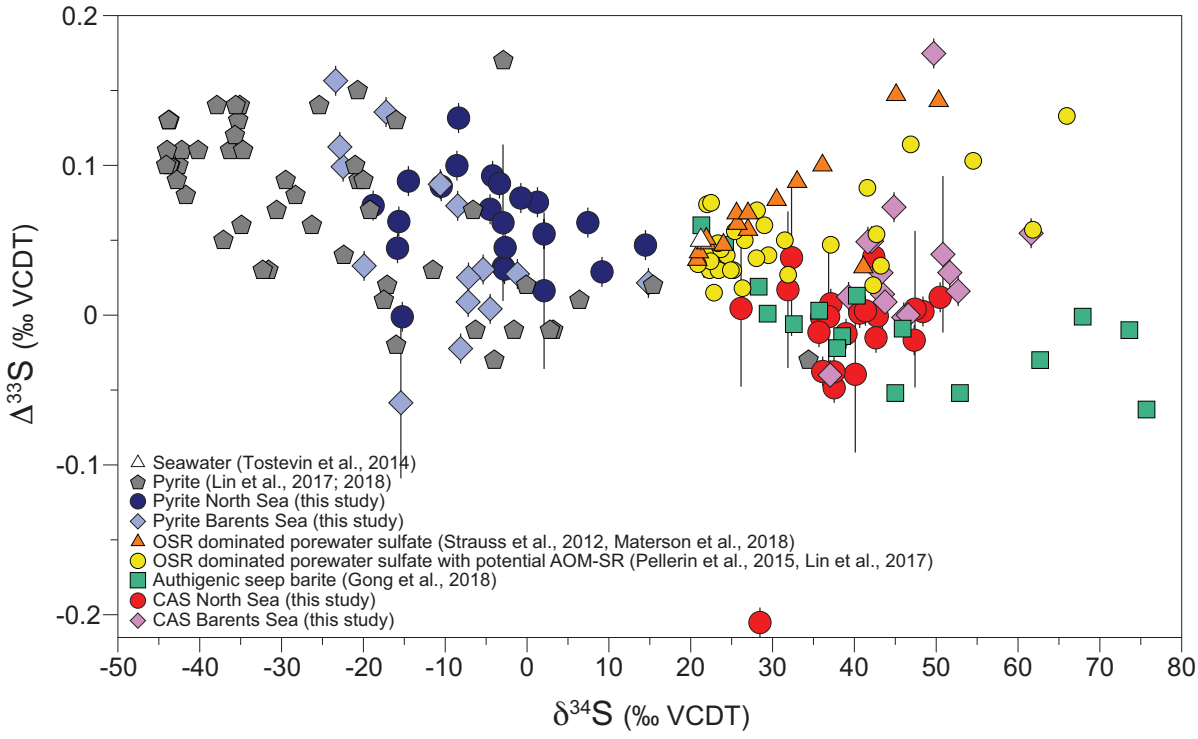

Figure 3: Plot of $\Delta^{33}S$ against $\delta^{34}S$ for pyrite, CAS, barite and pore water sulfate. Pyrite and CAS data from methane-derived authigenic carbonates from the North Sea and Barents Sea (this study) are compared to published porewater sulfate from marine sediments where organoclastic sulfate reduction (OSR) with and without the influence of anaerobic oxidation of methane coupled to sulfate reduction (AOM-SR; Lin et al., 2017, Pellerin et al., 2015, Strauss et al., 2012, Materson et al., 2018) as well as methane seep barite (Gong et al., 2018) and sedimentary pyrite influenced by OSR and AOM-SR (Lin et al., 2018, 2017). Analytical uncertainty (1σ) *on $\Delta^{33}S$ values are shown as vertical bars.*

The $\Delta^{33}S$ values of CAS range primarily between -0.048 and 0.072 ‰, with the exception of two data points ($\Delta^{33}S$ = 0.0175 ‰ and $\Delta^{33}S$ = -0.205 ‰) interpreted as outliers. In $\delta^{34}S$-$\Delta^{33}S$ space (Fig. 3), the CAS data are in relatively good agreement with previously measured seep barites (Gong et al., 2018). The CAS $\Delta^{33}S$ values are lower than porewater sulfate from sedimentary environments that are OSR dominated (Lin et al., 2017; Masterson et al., 2018; Pellerin et al., 2015; Strauss et al., 2012). While low $\Delta^{33}S$ values of sulfate are produced as a result of high metabolic SR rates that is potentially diagnostic of AOM-SR sustained by high methane fluxes (Gong et al., 2018), higher $\Delta^{33}S$ values associated with OSR in marine sediments most likely reflect a combination of lower metabolic SR rates, operating

266 closer to the thermodynamic equilibrium, as well as the influence of oxidative sulfur cycling
267 (Gong et al., 2018; Masterson et al., 2018; Pellerin et al., 2015).

268 The pyrite $\Delta^{33}S$ values range from -0.06 ‰ and 0.16 ‰ and converge towards
269 seawater values with increasing $\delta^{34}S$ (Fig. 3). MDAC petrography suggests that pyrite co-
270 occurs with the early generation microcrystalline carbonate cements whereas late generation
271 pure aragonite cavity fills that are found in higher volumetric fraction in the Barents Sea
272 MDACs contain typically very little or no pyrite. As such, seawater converging $\delta^{34}S$-$\Delta^{33}S$
273 values of pyrite in the North Sea may reflect relatively closer pore water system conditions
274 whereas pyrite precipitation in the Barents Sea may have occurred under relatively open
275 system and iron-limiting conditions. Although pyrites in MDACs are mostly ^{34}S-enriched
276 when compared to pyrites in sediments influenced by OSR (Fig. 3), there is no clear evidence
277 for a pattern of co-increasing $\Delta^{33}S$ and $\delta^{34}S$ values from AOM-SR as suggested by
278 sedimentary pyrite analysis from a deeper SMT (Lin et al., 2017).

279 ### *4.2. Evolving sulfate-sulfide multiple sulfur isotopes during AOM-SR*

280 In order to provide further constraints on the multiple sulfur isotope fractionation
281 associated with AOM-SR, a steady-state box model was developed following published
282 approaches (Johnston et al., 2005b; Kunzmann et al., 2017; Pellerin et al., 2015). The
283 objective was to constrain the multiple sulfur isotope evolution of sulfate and sulfide based on
284 the assumption that their respective sulfur isotope compositions are captured in CAS and
285 pyrite forming close to or at the sediment-water interface.

286 Fractionations which result from differential reaction rates of the isotopologues of sulfur
287 during sulfur transformations are describe as:

288 $$^{3i}R_{product} = {}^{3i}\alpha_{AOM-SR}\,{}^{3i}R_{reactant}$$

where ${}^{3i}R$ represents either the isotopic ratio $^{34}S/^{32}S$ or $^{33}S/^{32}S$, the subscripts *product* and *reactant* are self-explanatory and ${}^{3i}\alpha_{AOM-SR}$ represents the fractionation factor between product and reactant along a specific pathway. The relationship between ${}^{34}\alpha_{AOM-SR}$ and ${}^{33}\alpha_{AOM-SR}$ we establish as ${}^{33}\alpha_{AOM-SR} = {}^{34}\alpha_{AOM-SR}{}^{33\lambda}$. We assume that AOM-SR produces $^{34}\alpha_{\text{AOM-SR}}$ and $^{33}\lambda_{\text{AOM-SR}}$ similar to published culture experiments of sulfate reducers and vary these parameters in a linear relationship (Fig. S3, see also sensitivity tests illustrated in Fig. S4).

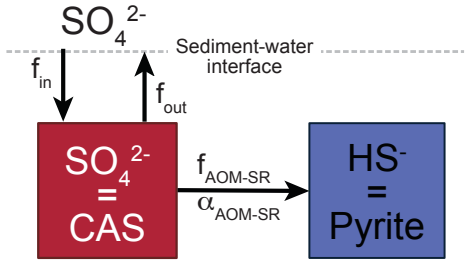

Figure 4: Schematic representation of the box model for AOM-SR. f_{in} and f_{out} represent the flux of porewater sulfate from and back to the overlying bottom water whereas $f_{AOM\text{-}SR}$ and ${}^{34/33}\alpha_{AOM\text{-}SR}$ the associated flux and sulfur isotopic fractions (^{34}S- ^{32}S and ^{33}S- ^{32}S), respectively. The model assumes that CAS and pyrite record porewater sulfate and sulfide, respectively, as well as no isotope fractionation associated with f_{in}, f_{out} and precipitation of CAS and pyrite.

We dissected the sulfur transformations which can take place in the sediments (Fig. 4) as follows: (1) a flux of sulfate from bottom water entering via diffusion or mixing into the sediment (f_{in}); (2) a flux of sulfate out of the sediment (f_{out}); and (3) a sulfide flux that becomes immobilized as pyrite (f_{AOM-SR}). We relax the assumption of a unidirectional sulfide flux later in our analysis. Support for reflux of porewater sulfate into bottom water comes from a number of studies where physical and biological irrigation processes have been shown to actively mix bottom water sulfate into the underlying sediments (e.g. Haeckel et al., 2007), particularly at dynamic seepage sites such as those where MDACs are forming. Assuming the fluxes are at steady state the mass balance on the fluxes is described by

$$f_{in} = f_{out} + f_{AOM-SR}$$

The net fractionation between the sulfate pool and pyrite can be described as

$$^{3i}\alpha_{net} = \frac{1}{F_{res}\left(\frac{1}{^{3i}\alpha_{AOM-SR}} - 1\right) + 1}$$

where $^{3i}\alpha_{net}$ is the isotopic ratio of the porewater sulfate relative to the pyrite deposited, $F_{AOM-SR} = (1 - \frac{f_{out}}{f_{in}})$ corresponds to the fraction of the sulfate entering the sediment which is consumed by AOM-SR and $^{3i}\alpha_{AOM-SR} = \frac{^{3i}R_{H_2S/pyrite}}{^{3i}R_{SO_4^{2-}/CAS}}$ represents the fractionation between the H_2S produced from sulfate reduction and the porewater sulfate pool (now preserved as pyrite and CAS respectively).

4.3. Decoupled precipitation of pyrite and carbonates

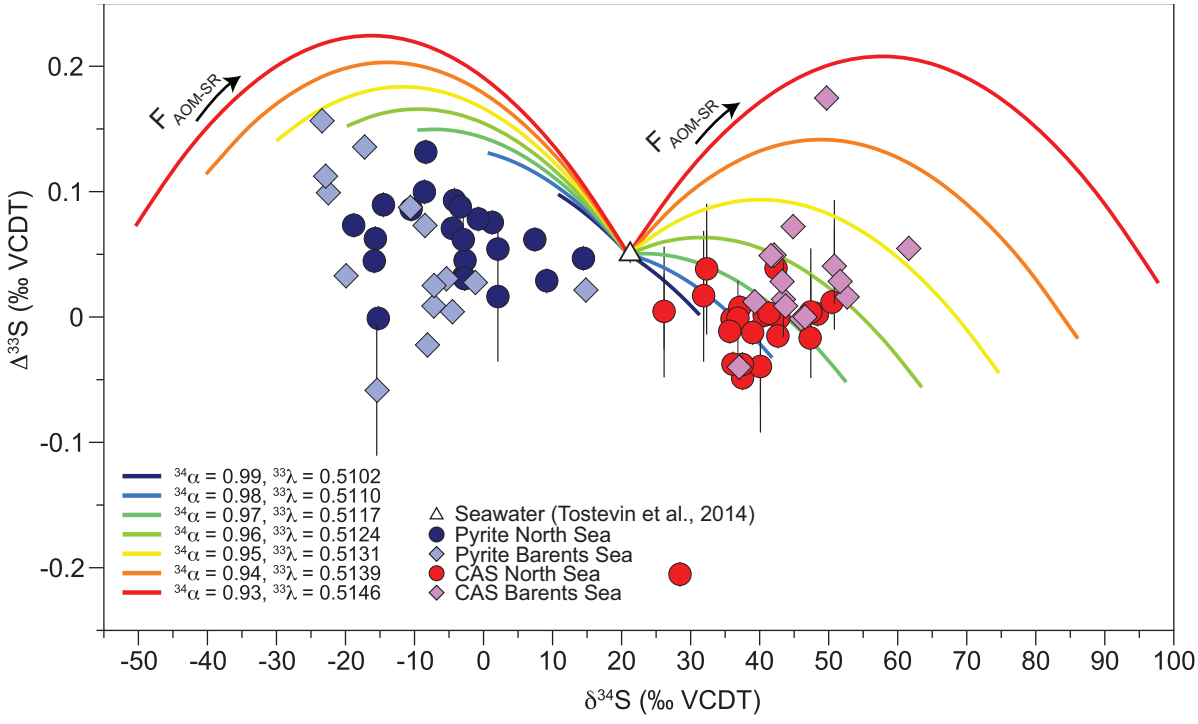

Figure 5: Modelled trajectories for fixed AOM-SR fractionation factors ($^{34}\alpha_{AOM-SR}$ ranging from 0.99 to 0.93) and varying the fraction of sulfate flux entering in the sediments that is consumed by AOM-SR (F_{AOM-SR} ranging from 0 to 1). Results are plotted on $\delta^{34}S$ and $\Delta^{33}S$ space and compared to measured pyrite and CAS extracted from methane-derived authigenic carbonates.

As shown in Fig. 5, the $\delta^{34}S$-$\Delta^{33}S$ trajectories for sulfate and sulfide from the steady-state box model become more concave with increasing fractionation factors. These model results cover most CAS data, which suggests that the precipitation of MDAC crusts occurred under a relatively limited range of sulfur isotopic discrimination, with $^{34}\alpha_{AOM\text{-}SR}$ from 0.99 to 0.96. Such low values of $^{34}\alpha_{AOM\text{-}SR}$ imply relative high rates of AOM-SR sustained by high methane flux (Aharon and Fu, 2000; Deusner et al., 2014). While this modelling exercise provides a consistent interpretation of the multiple sulfur isotope composition of CAS, the modelled field for pyrite is significantly higher than the measured $\delta^{34}S$-$\Delta^{33}S$ values for pyrite (Fig. 5). We interpret this discrepancy to indicate decoupled precipitation, at least partial, of pyrite from the CAS preserved in MDACs.

One possible reason for this decoupling is variable precipitation environments of pyrite. Pyrite co-precipitates in diagenetic realm with microcrystalline cements that are commonly Mg-calcite dominated. Assuming that CAS concentration in Mg-calcite is lower than aragonite (Feng et al., 2016), it appears likely that the contribution from carbonate phases that are co-genetic with pyrite is relatively minor to our bulk measurements. Hence, the CAS signal may be dominated by aragonite that forms under high methane flux and relatively open conditions where pyrite precipitation is less-favored. Considering the temporal variability in methane flux (Tryon et al., 2002) and that MDACs form over hundreds to few thousands of years (Crémière et al., 2016a, 2016b), the pyrite likely forms over protracted period of time and records an integrated signature of the sulfide. Changes in methane flux intensity results in vertical migration of the SMT and AOM-SR rates that can generate multiple pyrite precipitation episodes with a large range of sulfur isotopic compositions. Indeed, ion microprobe analysis of individual pyrite grains from the SMT shows large (> 30 ‰) microscale variability in $\delta^{34}S$ (Lin et al., 2016), supporting a protracted pyrite formation in these environments. To establish the range of $\delta^{34}S$ and $\Delta^{33}S$ values that may

result from time-integrated pyrite precipitation, we calculated mixing lines between sulfide end-members generated when sulfate flux entering the sediment is either quantitatively consumed or almost left unreacted ($F_{AOM\text{-}SR}$ values of 1 and 0, respectively) for a given fractionation factor (Fig. 6a). Such mixing field represents the maximum distribution of multiple sulfur isotope signatures that would be obtained when pyrite over time integrates the isotopic composition of variable porewater sulfide and shows that significantly lower $\Delta^{33}S$ values of pyrite can be attained than with AOM-SR alone, consistent with the observed isotopic compositions of the pyrites that we analyzed. However, the $^{34}\alpha_{AOM-SR}$ values required for this exercise are mostly above 0.96, that is much larger than the ones modelled for CAS, implying that pyrites could have formed over longer periods of time under much lower rates of AOM-SR from a transient deeper SMT.

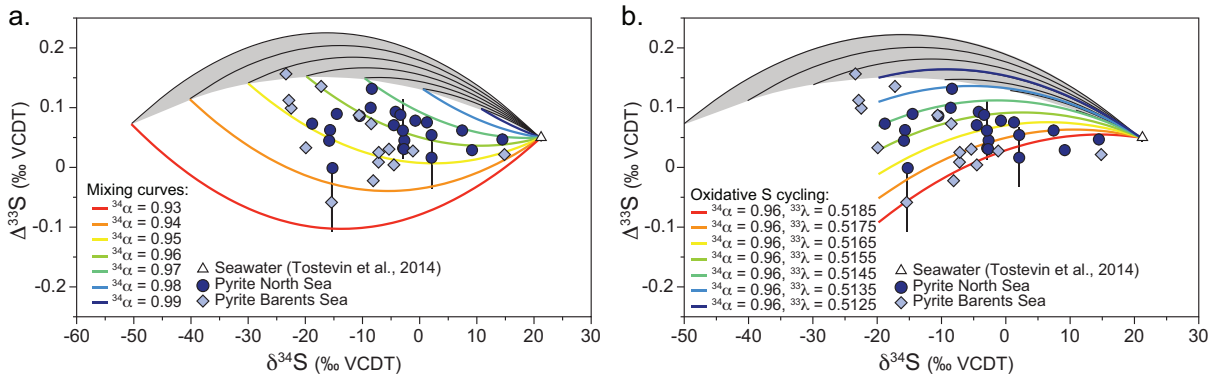

Figure 6: Impact of (a) sulfide mixing (between endmembers calculated for $F_{AOM\text{-}SR}$ = 0 and 1) and (b) of reoxidative sulfur cycling on pyrite from methane-derived authigenic carbonates (simulated by increasing $^{33}\lambda_{AOM\text{-}SR}$, note that values of $^{33}\lambda_{AOM\text{-}SR}$ above 0.518 would require near quantitative oxidation of sulfide produced by AOM-SR (Kunzmann et al., 2017)). The grey envelope represents results from the steady-state box model (see Fig. 5).

A second possibility is that an oxidative sulfur cycle, common in diagenetic regimes like the seep carbonate environment, that are characterized by non-steady-state (Aller et al., 2010), partially overprints the isotopic signature of AOM-SR that is preserved in pyrite from MDACs. Oxygen or nitrate in bottom waters and ferric/manganese oxyhydroxide minerals react abiotically and biologically with porewater sulfide, resulting in the production of sulfate or intermediate sulfur species in subsurface sediments (Jørgensen et al., 2019 and therein).

These intermediate sulfur species can be subsequently disproportionated microbially or oxidized back to sulfate in subsurface sediments (Lichtschlag et al., 2013) resulting in a distinct decrease in $\Delta^{33}S$ of sulfide than that produced by sulfate reduction alone (e.g. Pellerin et al., 2015, Johnston et al. 2005b). In addition, sulfur intermediate species accumulate in sulfidic porewater above the SMT (Lichtschlag et al., 2013), and may drive pyrite formation directly from sulfur intermediates. Following similar approaches (e.g. Johnston et al., 2005b; Kunzmann et al., 2017; Pellerin et al., 2015), the effect of an active oxidative sulfur cycle was artificially evaluated by taking into account a disproportionation loop between the porewater sulfate and sulfide pools by increasing $^{33}\lambda_{AOM\text{-}SR}$ for a given $^{34}\alpha_{AOM\text{-}SR}$. This leads to a decrease in the predicted $\Delta^{33}S$ of sulfide, also coherent with the measured pyrites in MDACs (Fig. 6b). Thus, the low $\Delta^{33}S$ values of studied pyrites may be attributed to an oxidative sulfur cycle in the seep carbonate environment. While the magnitude of sulfide oxidation, like a temporally changing porewater sulfide, probably depend on variations in methane flux, it is not possible to definitively separate the extent of both contributions to this dataset. The sulfur isotope signatures observed in pyrite appear to reflect a complex and unsteady sulfur cycle integrated over time, while CAS preserves sulfur isotopic signature that reflects AOM-SR metabolic activity and rapid MDAC precipitation close to the seafloor.

5. Conclusion

We analyzed the multiple sulfur isotopic compositions of paired CAS and pyrite in methane-derived authigenic carbonate crusts from the North Sea and Barents Sea which record the geochemical characteristics of porewater sulfate and sulfide at methane seeps. The CAS shows $\delta^{34}S$-$\Delta^{33}S$ values which, similar to recently published data from seep barites (Gong et al., 2018), are distinctly lower from sites where sulfate reduction coupled with sedimentary organic matter oxidation dominates. Mass-balance modelling shows that those CAS signatures are in

agreement with high metabolic rates of AOM-SR, sustained by high methane fluxes, leading to the precipitation of carbonate crusts close to the sediment-water interface. Our findings thus support that methane-derived authigenic carbonates contain CAS which multiple sulfur isotope signatures allow recognition of AOM-SR and make the distinction from OSR. However, modelled $\delta^{34}S$-$\Delta^{33}S$ field of pyrite is significantly higher than measured values suggesting that pyrite formation may be partly decoupled from carbonate precipitation. We propose that pyrite integrates the changing isotopic composition of sulfide which was controlled by a combination of porewater connectivity, methane flux variability and the oxidative sulfur cycle close to the sediment-water interface. Under these circumstances, the sulfide from which pyrite was formed is temporally and spatially variable and multiple sulfur isotopes fail in tracking the AOM-SR activity. Taken together, the multiple sulfur isotopes of CAS and pyrite preserved in methane-derived authigenic carbonates demonstrate the unsteady nature of sulfur cycling associated with methane seepage and carbonate formation.

Acknowledgements

This work was supported by Lundin Norway AS. We thank Thi Hao Bui and John Prince for analytical support.

Bibliography

Aharon, P., Fu, B., 2000. Microbial sulfate reduction rates and sulfur and oxygen isotope fractionations at oil and gas seeps in deepwater Gulf of Mexico. Geochim. Cosmochim. Acta 64, 233–246. https://doi.org/10.1016/S0016-7037(99)00292-6

Aller, R.C., Madrid, V., Chistoserdov, A., Aller, J.Y., Heilbrun, C., 2010. Unsteady diagenetic processes and sulfur biogeochemistry in tropical deltaic muds: Implications for oceanic isotope cycles and the sedimentary record. Geochim. Cosmochim. Acta 74, 4671–4692. https://doi.org/10.1016/j.gca.2010.05.008

Boetius, A., Ravenschlag, K., Schubert, C., Rickert, D., Widdel, F., Gieseke, A., Amann, R., Jørgensen, B., Witte, U., Pfannkuche, O., 2000. A marine microbial consortium apparently mediating anaerobic oxidation of methane. Nature 407, 623–626. https://doi.org/10.1038/35036572

Borowski, W.S., Rodriguez, N.M., Paull, C.K., Ussler III, W., 2013. Are 34S-enriched authigenic sulfide minerals a proxy for elevated methane flux and gas hydrates in the

geologic record? Mar. Pet. Geol. 43, 381–395. https://doi.org/10.1016/j.marpetgeo.2012.12.009

Bowles, M.W., Mogollon, J.M., Kasten, S., Zabel, M., Hinrichs, K.-U., 2014. Global rates of marine sulfate reduction and implications for sub-sea-floor metabolic activities. Science 344, 889–891. https://doi.org/10.1126/science.1249213

Brunner, B., Einsiedl, F., Arnold, G.L., Müller, I., Templer, S., Bernasconi, S.M., 2012. The reversibility of dissimilatory sulphate reduction and the cell-internal multi-step reduction of sulphite to sulphide: insights from the oxygen isotope composition of sulphate. Isotopes Environ. Health Stud. 48, 33–54. https://doi.org/10.1080/10256016.2011.608128

Claypool, G.E., Kvenvolden, K.A., 1983. Methane and other Hydrocarbon Gases in Marine Sediment. Annu. Rev. Earth Planet. Sci. 11, 299–327. https://doi.org/10.1146/annurev.ea.11.050183.001503

Crémière, A., Lepland, A., Chand, S., Sahy, D., Condon, D.J., Noble, S.R., Martma, T., Thorsnes, T., Sauer, S., Brunstad, H., 2016a. Timescales of methane seepage on the Norwegian margin following collapse of the Scandinavian Ice Sheet. Nat. Commun. 7.

Crémière, A., Lepland, A., Chand, S., Sahy, D., Kirsimäe, K., Bau, M., Whitehouse, M.J., Noble, S.R., Martma, T., Thorsnes, T., Brunstad, H., 2016b. Fluid source and methane-related diagenetic processes recorded in cold seep carbonates from the Alvheim channel, central North Sea. Chem. Geol. 432, 16–33. https://doi.org/10.1016/j.chemgeo.2016.03.019

Deusner, C., Holler, T., Arnold, G.L., Bernasconi, S.M., Formolo, M.J., Brunner, B., 2014. Sulfur and oxygen isotope fractionation during sulfate reduction coupled to anaerobic oxidation of methane is dependent on methane concentration. Earth Planet. Sci. Lett. 399, 61–73. https://doi.org/10.1016/j.epsl.2014.04.047

Doré, A., 1995. Barents Sea geology, petroleum resources and commercial potential. Arctic 207–221.

Egger, M., Riedinger, N., Mogollón, J.M., Jørgensen, B.B., 2018. Global diffusive fluxes of methane in marine sediments. Nat. Geosci. 11, 421–425. https://doi.org/10.1038/s41561-018-0122-8

Faleide, J.I., Vågnes, E., Gudlaugsson, S.T., 1993. Late Mesozoic-Cenozoic evolution of the south-western Barents Sea in a regional rift-shear tectonic setting. Mar. Pet. Geol. 10, 186–214. https://doi.org/10.1016/0264-8172(93)90104-Z

Farquhar, J., Johnston, D.T., Wing, B.A., Habicht, K.S., Canfield, D.E., Airieau, S., Thiemens, M.H., 2003. Multiple sulphur isotopic interpretations of biosynthetic pathways: implications for biological signatures in the sulphur isotope record. Geobiology 1, 27–36. https://doi.org/10.1046/j.1472-4669.2003.00007.x

Feng, D., Peng, Y., Bao, H., Peckmann, J., Roberts, H.H., Chen, D., 2016. A carbonate-based proxy for sulfate-driven anaerobic oxidation of methane. Geology G38233.1. https://doi.org/10.1130/G38233.1

Gong, S., Peng, Y., Bao, H., Feng, D., Cao, X., Crockford, P.W., Chen, D., 2018. Triple sulfur isotope relationships during sulfate-driven anaerobic oxidation of methane. Earth Planet. Sci. Lett. 504, 13–20. https://doi.org/10.1016/j.epsl.2018.09.036

Greinert, J., Bollwerk, S.M., Derkachev, A., Bohrmann, G., Suess, E., 2002. Massive barite deposits and carbonate mineralization in the Derugin Basin, Sea of Okhotsk: precipitation processes at cold seep sites. Earth Planet. Sci. Lett. 203, 165–180. https://doi.org/10.1016/S0012-821X(02)00830-0

Haeckel, M., Boudreau, B.P., Wallmann, K., 2007. Bubble-induced porewater mixing: A 3-D model for deep porewater irrigation. Geochim. Cosmochim. Acta 71, 5135–5154. https://doi.org/10.1016/j.gca.2007.08.011

Hovland, M., Judd, A.G., King, L.H., 1984. Characteristic features of pockmarks on the North Sea floor and Scotian Shelf. Sedimentology 31, 471–480.

Johnston, D.T., Farquhar, J., Wing, B.A., Kaufman, A.J., Canfield, D.E., Habicht, K.S., 2005a. Multiple sulfur isotope fractionations in biological systems: A case study with sulfate reducers and sulfur disproportionators. Am. J. Sci. 305, 645–660. https://doi.org/10.2475/ajs.305.6-8.645

Johnston, D.T., Wing, B.A., Farquhar, J., Kaufman, A.J., Strauss, H., Lyons, T.W., Kah, L.C., Canfield, D.E., 2005b. Active Microbial Sulfur Disproportionation in the Mesoproterozoic. Science 310, 1477–1479. https://doi.org/10.1126/science.1117824

Jørgensen, B.B., Böttcher, M.E., Lüschen, H., Neretin, L.N., Volkov, I.I., 2004. Anaerobic methane oxidation and a deep H_2S sink generate isotopically heavy sulfides in Black Sea sediments. Geochim. Cosmochim. Acta 68, 2095–2118. https://doi.org/10.1016/j.gca.2003.07.017

Jørgensen, B.B., Findlay, A.J., Pellerin, A., 2019. The Biogeochemical Sulfur Cycle of Marine Sediments. Front. Microbiol. 10. https://doi.org/10.3389/fmicb.2019.00849

Knittel, K., Wegener, G., Boetius, A., 2018. Anaerobic Methane Oxidizers, in: McGenity, T.J. (Ed.), Microbial Communities Utilizing Hydrocarbons and Lipids: Members, Metagenomics and Ecophysiology. Springer International Publishing, Cham, pp. 1–21. https://doi.org/10.1007/978-3-319-60063-5_7-1

Kunzmann, M., Bui, T.H., Crockford, P.W., Halverson, G.P., Scott, C., Lyons, T.W., Wing, B.A., 2017. Bacterial sulfur disproportionation constrains timing of Neoproterozoic oxygenation. Geology G38602.1. https://doi.org/10.1130/G38602.1

Lichtschlag, A., Kamyshny Jr., A., Ferdelman, T.G., deBeer, D., 2013. Intermediate sulfur oxidation state compounds in the euxinic surface sediments of the Dvurechenskii mud volcano (Black Sea). Geochim. Cosmochim. Acta 105, 130–145. https://doi.org/10.1016/j.gca.2012.11.025

Lin, Z., Sun, X., Peckmann, J., Lu, Y., Xu, L., Strauss, H., Zhou, H., Gong, J., Lu, H., Teichert, B.M.A., 2016. How sulfate-driven anaerobic oxidation of methane affects the sulfur isotopic composition of pyrite: A SIMS study from the South China Sea. Chem. Geol. 440, 26–41. https://doi.org/10.1016/j.chemgeo.2016.07.007

Lin, Z., Sun, X., Strauss, H., Lu, Y., Böttcher, M.E., Teichert, B.M.A., Gong, J., Xu, L., Liang, J., Lu, H., Peckmann, J., 2018. Multiple sulfur isotopic evidence for the origin of elemental sulfur in an iron-dominated gas hydrate-bearing sedimentary environment. Mar. Geol. 403, 271–284. https://doi.org/10.1016/j.margeo.2018.06.010

Lin, Z., Sun, X., Strauss, H., Lu, Y., Gong, J., Xu, L., Lu, H., Teichert, B.M.A., Peckmann, J., 2017. Multiple sulfur isotope constraints on sulfate-driven anaerobic oxidation of methane: Evidence from authigenic pyrite in seepage areas of the South China Sea. Geochim. Cosmochim. Acta 211, 153–173. https://doi.org/10.1016/j.gca.2017.05.015

Luff, R., Wallmann, K., Aloisi, G., 2004. Numerical modeling of carbonate crust formation at cold vent sites: significance for fluid and methane budgets and chemosynthetic biological communities. Earth Planet. Sci. Lett. 221, 337–353. https://doi.org/10.1016/S0012-821X(04)00107-4

Marenco, P., Corsetti, F., Hammond, D., Kaufman, A., Bottjer, D., 2008. Oxidation of pyrite during extraction of carbonate associated sulfate. Chem. Geol. 247, 124–132. https://doi.org/10.1016/j.chemgeo.2007.10.006

Masterson, A., Alperin, M.J., Berelson, W.M., Johnston, D.T., 2018. Interpreting multiple sulfur isotope signals in modern anoxic sediments using a full diagenetic model (California-Mexico margin: Alfonso Basin). Am. J. Sci. 318, 459–490. https://doi.org/10.2475/05.2018.02

528 Mazzini, A., Svensen, H.H., Planke, S., Forsberg, C.F., Tjelta, T.I., 2016. Pockmarks and
529 methanogenic carbonates above the giant Troll gas field in the Norwegian North Sea.
530 Mar. Geol. 373, 26–38. https://doi.org/10.1016/j.margeo.2015.12.012
531 McGlynn, S.E., Chadwick, G.L., Kempes, C.P., Orphan, V.J., 2015. Single cell activity
532 reveals direct electron transfer in methanotrophic consortia. Nature 526, 531–535.
533 https://doi.org/10.1038/nature15512
534 Nickel, J.C., di Primio, R., Mangelsdorf, K., Stoddart, D., Kallmeyer, J., 2012.
535 Characterization of microbial activity in pockmark fields of the SW-Barents Sea. Mar.
536 Geol. 332–334, 152–162. https://doi.org/10.1016/j.margeo.2012.02.002
537 Peckmann, J., Reimer, A., Luth, U., Luth, C., Hansen, B.T., Heinicke, C., Hoefs, J., Reitner,
538 J., 2001. Methane-derived carbonates and authigenic pyrite from the northwestern
539 Black Sea. Mar. Geol. 177, 129–150. https://doi.org/10.1016/S0025-3227(01)00128-1
540 Pellerin, A., Antler, G., Holm, S.A., Findlay, A.J., Crockford, P.W., Turchyn, A.V.,
541 Jørgensen, B.B., Finster, K., 2019. Large sulfur isotope fractionation by bacterial
542 sulfide oxidation. Sci. Adv. 5, eaaw1480. https://doi.org/10.1126/sciadv.aaw1480
543 Pellerin, A., Bui, T.H., Rough, M., Mucci, A., Canfield, D.E., Wing, B.A., 2015. Mass-
544 dependent sulfur isotope fractionation during reoxidative sulfur cycling: A case study
545 from Mangrove Lake, Bermuda. Geochim. Cosmochim. Acta 149, 152–164.
546 https://doi.org/10.1016/j.gca.2014.11.007
547 Rise, L., Bellec, V.K., Chand, S., Bøe, R., 2014. Pockmarks in the southwestern Barents Sea
548 and Finn mark fjords. Nor. J. Geol. 94, 263–282.
549 Ruppel, C.D., Kessler, J.D., 2017. The interaction of climate change and methane hydrates.
550 Rev. Geophys. 55, 2016RG000534. https://doi.org/10.1002/2016RG000534
551 Sauer, S., Hong, W., Knies, J., Lepland, A., Forwick, M., Klug, M., Eichinger, F., Baranwal,
552 S., Crémière, A., Chand, S., 2016. Sources and turnover of organic carbon and
553 methane in fjord and shelf sediments off northern Norway. Geochem. Geophys.
554 Geosystems 17, 4011–4031.
555 Sim, M.S., Bosak, T., Ono, S., 2011. Large sulfur isotope fractionation does not require
556 disproportionation. Science 333, 74–77. https://doi.org/10.1126/science.1205103
557 Strauss, H., Bast, R., Cording, A., Diekrup, D., Fugmann, A., Garbe-Schönberg, D., Lutter,
558 A., Oeser, M., Rabe, K., Reinke, D., Teichert, B.M.A., Westernströer, U., 2012.
559 Sulphur diagenesis in the sediments of the Kiel Bight, SW Baltic Sea, as reflected by
560 multiple stable sulphur isotopes. Isotopes Environ. Health Stud. 48, 166–179.
561 https://doi.org/10.1080/10256016.2012.648930
562 Tostevin, R., Turchyn, A.V., Farquhar, J., Johnston, D.T., Eldridge, D.L., Bishop, J.K.B.,
563 McIlvin, M., 2014. Multiple sulfur isotope constraints on the modern sulfur cycle.
564 Earth Planet. Sci. Lett. 396, 14–21. https://doi.org/10.1016/j.epsl.2014.03.057
565 Tryon, M.D., Brown, K.M., Torres, M.E., 2002. Fluid and chemical flux in and out of
566 sediments hosting methane hydrate deposits on Hydrate Ridge, OR, II: Hydrological
567 processes. Earth Planet. Sci. Lett. 201, 541–557. https://doi.org/10.1016/S0012-
568 821X(02)00732-X
569 Wallmann, K., Drews, M., Aloisi, G., Bohrmann, G., 2006. Methane discharge into the Black
570 Sea and the global ocean via fluid flow through submarine mud volcanoes. Earth
571 Planet. Sci. Lett. 248, 545–560. https://doi.org/10.1016/j.epsl.2006.06.026
572 Wegener, G., Krukenberg, V., Riedel, D., Tegetmeyer, H.E., Boetius, A., 2015. Intercellular
573 wiring enables electron transfer between methanotrophic archaea and bacteria. Nature
574 526, 587–590. https://doi.org/10.1038/nature15733
575 Wilkin, R.T., Barnes, H.L., 1996. Pyrite formation by reactions of iron monosulfides with
576 dissolved inorganic and organic sulfur species. Geochim. Cosmochim. Acta 60, 4167–
577 4179. https://doi.org/10.1016/S0016-7037(97)81466-4

578 Wing, B.A., Halevy, I., 2014. Intracellular metabolite levels shape sulfur isotope fractionation
579 during microbial sulfate respiration. Proc. Natl. Acad. Sci. 111, 18116–18125.
580 https://doi.org/10.1073/pnas.1407502111
581 Winsborrow, M.C.M., Andreassen, K., Corner, G.D., Laberg, J.S., 2010. Deglaciation of a
582 marine-based ice sheet: Late Weichselian palaeo-ice dynamics and retreat in the
583 southern Barents Sea reconstructed from onshore and offshore glacial geomorphology.
584 Quat. Sci. Rev. 29, 424–442. https://doi.org/10.1016/j.quascirev.2009.10.001
585